Development of an adaptive CTM-RPIM method for modelling large deformation problems in geotechnical engineering

Jianguo Li[a,b], Bin Wang[a,b*], Quan Jiang [a,b*], Benguo He[c], Xue Zhang[d], Philip J. Vardon[e]

[a] *State Key Laboratory of Geomechanics and Geotechnical Engineering, Institute of Rock and Soil Mechanics, Chinese Academy of Sciences, Wuhan, China*

[b] *University of Chinese Academy of Sciences, Beijing, China*

[c] *Key Laboratory of Ministry of Education on Safe Mining of Deep Metal Mines, Northeastern University, China*

[d] *Department of Civil Engineering and Industrial Design, University of Liverpool, Liverpool, UK*

[e] *Geo-engineering Section, Delft University of Technology, Delft, the Netherlands*

Corresponding author: Bin Wang; bwang@whrsm.ac.cn

Co-corresponding author: Quan Jiang; qjiang@whrsm.ac.cn

Abstract

In this paper, a meshfree method namely adaptive CTM-RPIM is developed for modelling geotechnical problems with large deformations. The developed adaptive CTM-RPIM is a combination of the Cartesian transformation method (CTM), the radial point interpolation method (RPIM) and the alpha shape method. To reduce the requirement of meshes, the CTM is adopted to transform domain integrals into line integrals and RPIM is applied to construct interpolation functions. The alpha shape method, which is capable of capturing the severe boundary evolution due to large deformations, is then introduced into the CTM-RPIM to form the adaptive CTM-RPIM. The accuracy of CTM-RPIM is first verified by considering a cantilever beam under small deformation, where the influence of key parameters on simulation results is explored. Afterwards, the ability of the adaptive CTM-RPIM for handling large deformation problems is demonstrated by simulating cantilever beams with large deformations for which analytical solutions are available. In addition, a slope failure problem and a footing bearing capability problem are modelled to illustrate the ability of evaluating the stability of geotechnical structures. Finally, a 2-D soil collapse experiment using small aluminum bars is simulated to test its capability of simulating geotechnical large deformation problems. These benchmark examples show that the adaptive CTM-RPIM is a numerical method of broad application prospect.

Keywords: Cartesian transformation method; Radial point interpolation method; Alpha shape method; Large deformation; Geotechnical engineering.

1. Introduction

The occurrence of many natural disasters, such as landslides, earthquakes, debris flows and so on, are often accompanied by large and severe deformations [1-3]. Many numerical methods have been developed to solve these problems, but some of them may encounter some problems, such as mesh entanglement and inconsistency between integral domain and problem domain, etc.

When dealing with large deformation problems, to some mesh based methods such as the finite element method (FEM) [4, 5] and the finite difference method (FDM) [6, 7], remesh, a time consuming operation, is necessary to avoid mesh distortion. To overcome the reliability of mesh, various meshfree methods have been developed. However, background mesh is used in some classical meshfree method to facilitate the integration of stiffness matrix and force vector etc. Take the material point method (MPM) [8, 9] and the element free Galerkin method (EFGM) [10-12] for example, the use of background mesh will result in the inconsistency between the integral domain and the problem domain, which may cause errors when the model is rough. In addition, this may bring up a problem in MPM that may increase the computational cost, that is, at each step, you need to judge which background cell the integral point is located in. Some meshfree methods without background mesh may also have minor disvantages, such as the meshfree local Petrov-Galerkin method (MLPG) [13]. In MLPG, the weak form of governing equation is established by local Petrov-Galerkin method, which may lead to the asymmetry of stiffness matrix and increase the computational time. Summing up the above, a meshfree method without background mesh, using Galerkin method to construct its weak form and having coincident problem domain and integral domain can be developed to avoid these disadvantages.

The Cartesian transformation method (CTM) [14, 15], originating from the boundary element method (BEM) [16], is an integral method that can transform domain integration into a boundary integration and a 1-D integration. This means that mesh or background mesh will not be needed when computing the integration of stiffness matrix and force vector, and the integral domain will coincides with the problem domain, if CTM is used. The radial point interpolation method (RPIM) [17-19] is of high precision for scattered data interpolation, which can get rid of the restriction of mesh when constructing the shape functions. Moreover, RPIM has a simple theory basis, which is easy to implement with programming and extend to 3-D space. It is conceivable that the combination of CTM and RPIM in the governing equation based on Galerkin method would result in a truly meshfree method with symmetrical stiffness matrix and coincident problem domain and integral domain.

Another problem in dealing with geotechnical large deformation problems is to track the boundary of problem domain when severe deformations occur. The boundary tracking accuracy has great influence on the result, and one of the easiest ways to search the boundary (surface) of point cloud is using the alpha shape method. The reliability of alpha shape method [20] has already been proved in particle finite element method (PFEM) [21] and smooth particle finite element method (SPFEM) [22-24], in which alpha shape method is used to identify the boundary with Delaunay triangularization. The adaptive procedure can be constructed by tracking the boundary as the growth of deformation.

In this paper, to solve the geotechnical large deformation problems, an adaptive CTM-RPIM is formulated, which combines CTM, RPIM and the alpha shape method. The motivation of developing this new method, is to try to incorporate the merits of each method. RPIM basically is a meshfree method, which can model the large deformations, but the key problem is to find an appropriate support domain for each integration point to ensure the numerical stability. Mesh-based method has its advantages in dealing with the numerical integrations, however, it may encounter the mesh entanglement, or the strong rely on the background mesh, resulting in problems of the accurate capture of the material domain as shown in MPM. CTM is a way of transferring the domain integrations into the line integrals, which greatly reduce the requirements of searching for a support domain of each integration point. Thereby, by combining the two methods, it still inherits the advantages of the meshfree method for its capabilities of modelling the large deformations, more importantly, by utilizing the CTM integration algorithm, the numerical stabilities can be improved with a relatively convenient way, i.e. transferring the domain integration into the line integrals. An external algorithm, i.e. the alpha shape method, is incorporated, which allows the accurate track of the boundary for the dynamic process of large deformation. It is noted that, the boundary identification may be avoided, via the use of CTM integration in regular regions inside the object, and nodal integrations outside this region, as seen in EFGM [1].

The whole paper is mainly organized in three parts. Firstly, a brief introduction of the adaptive CTM-RPIM is given first, and the formulation of CTM and RPIM as well the procedure of alpha shape method is then presented. Key parameters of CTM and RPIM, regarding to the computational accuracies, are studied, and the optimal parameters are determined and suggested. Secondly, two large deformation examples of cantilever beams are carried out to verify the advantages of this method for large deformation problems. Finally, three geotechnical examples including slope stability, foundation capability and soil flow are shown, which proves the reliability of this method.

2. Formulation and implementation procedure of the adaptive CTM-RPIM

A detailed introduction to the development of the adaptive CTM-RPIM is carried out in this section. The governing equation and the implementation procedure of adaptive CTM-RPIM are provided to help reads to understand how it works. After that, the computational steps for programming are presented, which include both quasi static version and dynamic version. Finally the formulations of CTM, the construction of RPIM shape functions and the procedure of alpha shape method are illustrated in detail respectively for further understanding to the reader.

2.1. Implementation procedure of adaptive CTM-RPIM

2.1.1 The governing equation

The mechanical behavior of soil usually obeys the governing equation of continuum mechanics, which can be derived from the momentum conservation equation.

$$\nabla \boldsymbol{\sigma} + \boldsymbol{b} = \rho \ddot{\boldsymbol{u}} \tag{1}$$

Where ∇ is the partial differential operator; $\boldsymbol{\sigma}$ is the stress vector; $\boldsymbol{b}$ is the boundary condition; ρ is the density of material and $\ddot{\boldsymbol{u}}$ is the acceleration.

To solve this partial differential equation (PDE), Galerkin method can be used to form its weak form by introducing a test function $\delta \boldsymbol{u}$ in to Eq. (1).

$$\int_\Omega \delta \boldsymbol{u} : \boldsymbol{\sigma} d\Omega - \int_\Omega \delta \boldsymbol{u} \cdot \boldsymbol{f}^b d\Omega - \int_\Gamma \delta \boldsymbol{u} \cdot \boldsymbol{f}^\Gamma d\Gamma = \int_\Omega \delta \boldsymbol{u} \cdot \rho \ddot{\boldsymbol{u}} d\Omega \tag{2}$$

Where $\boldsymbol{f}^b$ is the body force and $\boldsymbol{f}^\Gamma$ is the surface force. The above equation is a conservation equation of virtual energy. The first term at the left-hand side is caused by internal force, the second and third term is caused by external force and the term at the right-hand side is caused by inertia force.

To solve Eq. (2), the discrete form should be constructed just like the way in standard FEM, and the adaptive procedure should be established to deal with large deformation problems. These will be given in the next three section.

2.1.2 Adaptive procedure for large deformations

How to combine the alpha shape method, CTM and RPIM to construct an adaptive procedure that can be automatically executed during large deformations will be explained in this section. In this procedure, the CTM-RPIM is used to establish the discrete form of momentum conservation equation and the alpha shape method is used to track the boundary when the configuration is updated. A simple schematic diagram is given in Fig.1 to help readers to understand this procedure.

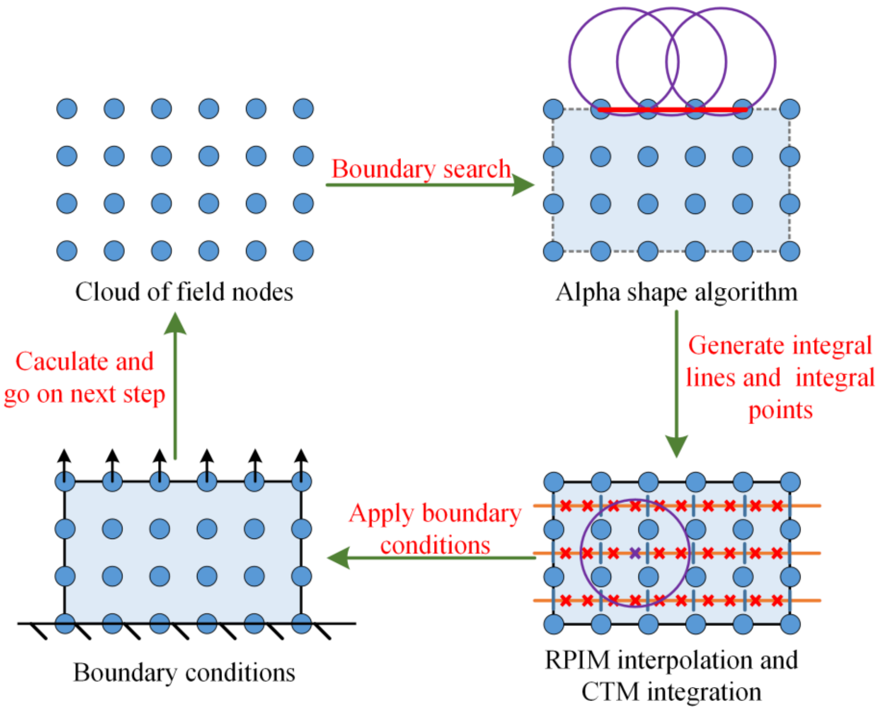

Fig. 1. The implementation procedure of adaptive CTM-RPIM

As shown in Fig.1, the adaptive CTM-RPIM for large deformation analysis can be divided into four basic steps.

(1) Search the boundary of the field nodes cloud to determine the scope of problem domain and integral domain.

(2) Generate integral lines and integral points, and form the stiffness matrix, mass matrix and force vector.

(3) Apply boundary conditions to establish the discretized equation to be solved.

(4) Solve the equation formed in step (3), then delete the previous boundary, and the problem domain still returns to the state represented by field nodes.

Repeat the above four steps until the error of displacement, force, or energy between two adjacent steps is tolerable.

It is clear that remesh operation is not required in the proposed adaptive CTM-RPIM. Only boundary identification is carried out using alpha shape method, so there will be no problems caused by mesh distortion. Moreover, the integral domain is consistent with the problem domain, which is helpful to accuracy. Additionally, in contrast to the EFGM and the traditional RPIM, there is no need to check whether the integral points are in the problem domain. Furthermore, comparing with MPM, there is no need to find which background cell an integral point is in.

2.1.3 Computational steps for quasi static problems

For quasi static problems, the acceleration can be ignored, so that the right-hand term of Eq. (2) is eliminated. The governing equation can be rewritten as:

$$\int_{\Omega} \delta \boldsymbol{u} : \boldsymbol{\sigma} d\Omega = \int_{\Omega} \delta \boldsymbol{u} \cdot \boldsymbol{f}^{b} d\Omega + \int_{\Gamma} \delta \boldsymbol{u} \cdot \boldsymbol{f}^{\Gamma} d\Gamma \tag{3}$$

This is a form commonly found in standard FEM, which can be discrete by assuming a relationshape between the variables of concerned point and the variables on field nodes using shape functions. Following the similar process of standard FEM, the discretized global equilibrium equation can be derived.

$$\boldsymbol{KU} = \boldsymbol{F}_{ext} \tag{4}$$

Where $\boldsymbol{K}$ is the global stiffness matrix, and $\boldsymbol{F}_{ext}$ is the global external force vector. Using CTM integration the detailed expression of each term can be obtained.

$$\boldsymbol{K} = \sum_{i=1}^{m} \boldsymbol{B}_i^T \boldsymbol{D}_i \boldsymbol{B}_i w_i^x w_i^y J_i^x J_i^x \tag{5}$$

$$\boldsymbol{F}_{ext} = \sum_{i=1}^{m} \boldsymbol{N}_i \boldsymbol{f}_i^b w_i^x w_i^y J_i^x J_i^x + \sum_{j=1}^{mb} \boldsymbol{N}_j \boldsymbol{f}_j^{\Gamma} w_j J_j \tag{6}$$

Where m is the number of integral points, $\boldsymbol{B}_i$ is the matrix of partial derivative of shape functions at i^{th} integral point, $\boldsymbol{N}_i$ is RPIM shape function matrix at i^{th} integral point, w_i^x, w_i^y, J_i^x, J_i^x are the weight and Jacobi determinant in *x* and *y* directions of i^{th} integral point. The second term in $\boldsymbol{F}_{ext}$ has a similar meaning, except that it is in the form of a boundary integration, which can be solved using Gaussian integral method.

Moreover the expression of internal force, which is another expression of $\boldsymbol{KU}$ in Eq. (4), can also be derived from the left-hand term of Eq. (3).

$$\boldsymbol{F}_{int} = \sum_{i=1}^{m} \boldsymbol{B}_i \boldsymbol{\sigma}_i w_i^x w_i^y J_i^x J_i^x \tag{7}$$

To solve Eq. (4), Newton-Raphson iteration is often used. And the quasi static version of adaptive CTM-RPIM is given here for material nonlinearity example with small deformation or weightless material with large deformation. The adaptive procedure is as follow

(1) Discrete the problem domain using a series of field nodes.

(2) Loop over the incremental step (n^{th} incremental step).

(3) Search the boundary of problem domain based on the cloud of field nodes using the alpha shape method.

(4) Generate the integral lines and integral points and form the total external force vector $\boldsymbol{F}_{ext}^n$ for the present incremental step.

(5) Loop over Newton-Raphson iteration (l^{th} iteration step).

(6) Form the global stiffness matrix $\boldsymbol{K}_l^n$ and the global internal force vector $\boldsymbol{F}_{int(l)}^n$.

(7) Solve the governing equation $\boldsymbol{K}_l^n \boldsymbol{U}_l^n = \boldsymbol{F}_{ext}^n - \boldsymbol{F}_{int(l)}^n$.

(8) Check convergence.

If it is converged, go to step 10.

(9) End looping the Newton-Raphson iteration.

(10) Check the incremental step limit.

If the incremental step is more than the limit, update the configuration and go to step (12).

If the incremental step is less than the limit, update the configuration and go to step (2).

(11) End looping the incremental step.

(12) Post processing.

2.1.4 Computational steps for dynamic problems

For dynamic problems, if weight is taken into account, the acceleration can’t be ignored. The left and right hands of Eq. (2) can be swapped to make it more suitable for constructing the format of time integral.

$$\int_{\Omega}\delta\boldsymbol{u}\cdot\rho\ddot{\boldsymbol{u}}d\Omega=\int_{\Omega}\delta\boldsymbol{u}:\boldsymbol{\sigma}d\Omega-\int_{\Omega}\delta\boldsymbol{u}\cdot\boldsymbol{f}^{b}d\Omega-\int_{\Gamma}\delta\boldsymbol{u}\cdot\boldsymbol{f}^{\Gamma}d\Gamma \tag{8}$$

In the similar way of standard FEM, the discrete momentum conservation can be derived from Eq. (8).

$$\boldsymbol{M}\ddot{\boldsymbol{U}}=\boldsymbol{F}_{ext}-\boldsymbol{F}_{int} \tag{9}$$

Where $\boldsymbol{M}$ is the mass matrix, and $\ddot{\boldsymbol{U}}$ is the acceleration vector. The lumped matrix is used here to improve the computational efficiency.

Sometimes, damping force can be introduced into Eq. (9) for the convergence rate and stability of the program.

$$\boldsymbol{M}\ddot{\boldsymbol{U}}=\boldsymbol{F}_{ext}-\boldsymbol{F}_{int}+\boldsymbol{F}_{damp} \tag{10}$$

Where $\boldsymbol{F}_{damp}$ is the damping force vector, which can be expressed as follow, if the local damping is used.

$$\boldsymbol{F}_{damp}=-f\left|\boldsymbol{F}_{ext}-\boldsymbol{F}_{\mathrm{int}}\right|sign(\dot{\boldsymbol{U}}) \tag{11}$$

Where f is the damping factor and $\dot{\boldsymbol{U}}$ is the velocity vector, which can be determined by central difference method.

The detailed procedures with explicit time integral are given as follow for dynamic problems with both geometric nonlinearity and material nonlinearity.

(1) Discrete the problem domain using a series of field nodes.

(2) Start time step *n*.

(3) Tracking the boundary using alpha shape method.

(4) Generate the integral lines and integral points

A. compute the total force vector at time t^n : $\boldsymbol{F}^{n}=\boldsymbol{F}_{ext}^{n}-\boldsymbol{F}_{int}^{n}+\boldsymbol{F}_{damp}^{n}$.

B. compute the mass matrix at time t^n : $\boldsymbol{M}^{n}$

(5) Calculate the acceleration vector at time t^n: $\ddot{\boldsymbol{U}}^{n}=(\boldsymbol{M}^{n})^{-1}\boldsymbol{F}^{n}$

(6) Calculate the velocity vector at time $t^{n+1/2}$: $\dot{\boldsymbol{U}}^{n+1/2} = \dot{\boldsymbol{U}}^{n-1/2} + \Delta t^n \ddot{\boldsymbol{U}}^n$, where $\Delta t^n = t^{n+1/2} - t^{n-1/2}$.

(7) Calculate the displacement vector at time t^{n+1} : $\boldsymbol{U}^{n+1} = \boldsymbol{U}^n + \Delta t^{n+1/2} \dot{\boldsymbol{U}}^{n+1/2}$, where $\Delta t^{n+1/2} = t^{n+1} - t^n$.

(8) Calculate the internal force vector at time t^{n+1}: $\boldsymbol{F}_{int}^{n+1}$

(9) Update the configuration use the displacement vector $\boldsymbol{U}^{n+1}$.

(10) Check converge or check limit.

If converged or reached the time step limit, end the calculation, otherwise go to the step (2) and start the $n+1$ time step

2.2. Formulation of CTM

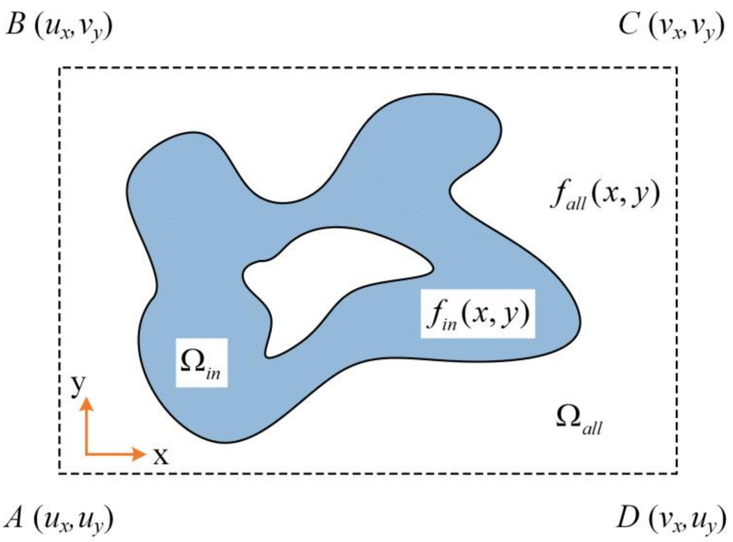

Fig. 2. A domain integration of the function $f_{in}(x, y)$

CTM is a special integration method originally applied in BEM [16]. Here, it is introduced into the meshfree method to form the stiffness matrix, mass matrix and force vector. Consider an integration I_{in} of a function $f_{in}(x, y)$ over a domain Ω_{in}

$$I_{in} = \int_{\Omega_{in}} f_{in}(x, y) dxdy \tag{12}$$

As shown in Fig. 2, the domain is so complex that the integration cannot carried out directly. To solve Eq. (12), a rectangular auxiliary domain Ω_{all} is constructed, which contains fully the domain over which the integration must take place. The function in the rectangular auxiliary domain, $f_{all}(x,y)$, can then be expressed as

$$f_{all}(x,y)=\begin{cases} f_{in}(x,y) & (in\ \Omega_{in}) \\ 0 & (out\ of\ \Omega_{in}) \end{cases} \tag{13}$$

and the integration I_{in} is rewritten as

$$I_{in}=\int_{\Omega_{all}} f_{all}(x,y)dxdy \tag{14}$$

Assuming that the function $h_{all}(x,y)$ is the integration of $f_{all}(\xi,y)$

$$h_{all}(x,y)=\int_c^x f_{all}(\xi,y)d\xi \tag{15}$$

Where ξ is a variable independent of *x* and *y* and *c* is an arbitrary constant. Adoping Green's theorem, Eq. (14) can be expressed as

$$\begin{aligned} I_{in} &= \int_{\Gamma_{all}} h_{all}(x,y)dy \\ &= \int_{\Gamma_{all}} (\int_c^x f_{all}(\xi,y)d\xi)dy \\ &= \int_{\Gamma_{AB+BC+CD+DA}} (\int_c^x f_{all}(\xi,y)d\xi)dy \end{aligned} \tag{16}$$

For a rectangular auxiliary domain Ω_{all}, dy is zero on boundary *DA* and *BC*. By setting *c* to be u_x, $\int_c^x f_{all}(\xi,y)d\xi$ will be zero on boundary *AB* implying that the integration in Eq. (16) only needs to be caculated on boundary *CD*

$$\begin{aligned} I_{in} &= \int_{\Gamma_{CD}} (\int_{u_x}^x f_{all}(\xi,y)d\xi)dy \\ &= \int_{\Gamma_{CD}} (\int_{u_x}^{v_x} f_{all}(\xi,y)d\xi)dy \\ &= \int_{u_y}^{v_y} (\int_{u_x}^{v_x} f_{all}(x,y)dx)dy \end{aligned} \tag{17}$$

The above integration can be divided as following

$$I_{in}=\int_{u_y}^{v_y} g(y)dy \tag{18}$$

$$g(y)=\int_{u_x}^{v_x} f_{all}(x,y)dx \tag{19}$$

To caculate these two integrations, a series of integral lines are introduced as shown in Fig. 3. Then the integration I_{in} can be evaluated based on some numerical integration methods, such as

Gauss integration, and the value of i^{th} integral line is $g(y_i)$.

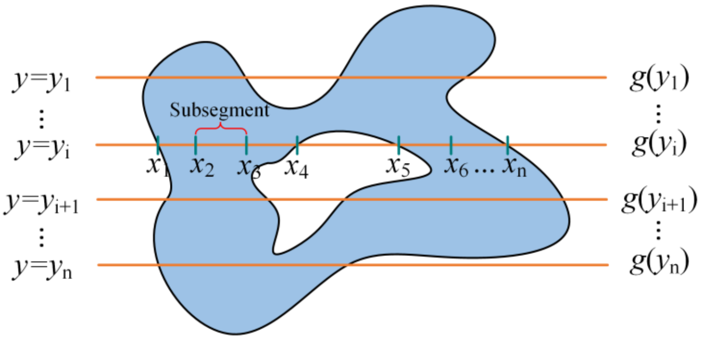

Fig. 3. CTM integral scheme

By dividing the i^{th} integral line into n-1 segments, $g(y_i)$ can be caculated as

$$
\begin{aligned}
g(y_i) &= \int_{x_1}^{x_n} f_{all}(x, y_i)dx \\
&= \sum_{j=2}^{n} (\int_{x_{j-1}}^{x_j} f_{all}(x, y_i)dx)
\end{aligned}
\tag{20}
$$

Recalling the relationship between f_{all} and f_{in}, $g(y_i)$ can also be expressed in terms of f_{in}. If f_{in} is used, the integration $\int_{x_4}^{x_5} f_{in}(x, y_i)dx$ vanishes in Fig. 3 and $g(y_i)$ is written as

$$
g(y_i) = \sum_{j=2}^{n} (\int_{x_{j-1}}^{x_j} f_{in}(x, y_i)dx) \qquad (j \neq 5) \tag{21}
$$

Similar to the evaluation of I_{in}, $g(y_i)$ can be calculated numerically. Using Gauss integration scheme, we have

$$
I_{in} = \sum_{i=1}^{m_y} g(y_i) \cdot w_i^y \cdot J_i^y \tag{22}
$$

where m_y represents the total number of integral lines, w_i^y and J_i^y are the weight and Jacobi determinant along y direction, respectively, and

$$
g(y_i) = \sum_{j_x=1}^{m_x} f_{in}(x_{j_x}, y_i) \cdot w_{j_x}^x \cdot J_{j_x}^x \tag{23}
$$

where m_x is the total number of integral points on each integral line, $w_{j_x}^x$ and $J_{j_x}^x$ are the weight and Jacobi determinant along x direction, respectively.

Substituting Eq. (23) into (22) leads to the final form of I_{in}

$$I_{in} = \sum_{k=1}^{m} f_{in}(x_k, y_k) \cdot w_k^x \cdot w_k^y \cdot J_k^x \cdot J_k^y \tag{24}$$

which is the sum of the produce of the function at integral points and the corresponding weight and Jacobi determinant in two directions. Where k is the global number of integral points, and m is the total number of integral points. As such the CTM trasforms domain integration into line integration. Consequently, only the intersections of integral lines and boundary are needed in the simulation leading to a truly meshfree method with coincident problem domain and integral domain. Eq. (24) is exactly the numerical integration version used in Section 2.1 to caculate the stiffness matrix, mass matrix and force vector.

2.3. RPIM based shape functions

Generally, the problem domain is represented by a series of field nodes in meshfree methods. Because of the adoption of the CTM, there is no background mesh and thus shape functions should be constructed based on the field nodes. In this paper, the RPIM is used for this purpose which is introduced as below.

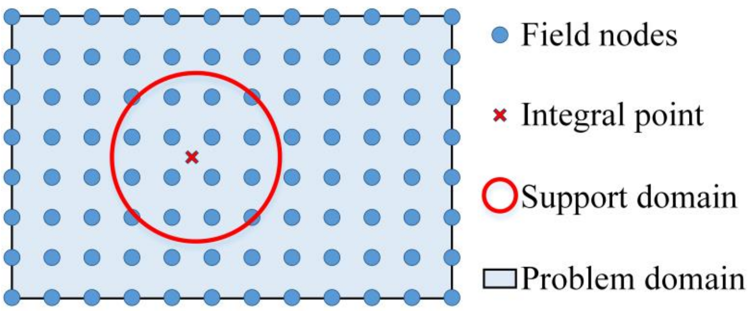

Fig.4. The support domain in RPIM

For an arbitrary integral point, a support domain can be formed as shown in Fig. 4. The shape of the support domain can be circular or rectangular. Supposing that the support domain covers n field nodes, the field variable, $F(x, y)$, at the concerned point can be approximated by

$$F(x, y) = \begin{bmatrix} \boldsymbol{R}^T(r(x, y)) & \boldsymbol{P}^T(x, y) \end{bmatrix} \begin{bmatrix} \boldsymbol{A} \\ \boldsymbol{B} \end{bmatrix} \tag{25}$$

where $\boldsymbol{R}^T(r(x, y)) = \begin{bmatrix} r_1(x, y) & r_2(x, y) & \dots & r_n(x, y) \end{bmatrix}$ is the vector consisting of the radial basis function (RBF) with $r_i(x, y)$ being the distance between the point at (x, y) and the field node at

(x_i, y_i) in two-dimensional cases, $\boldsymbol{P}^T(x, y) = \begin{bmatrix} 1 & x & y & xy & x^2 & y^2 & ... \end{bmatrix}$ is the vector of polynomial basis functions, and $\boldsymbol{A}$ and $\boldsymbol{B}$ are row vectors of constants to be determined. Eq. (25) has to be satisfied at all field nodes. For example, the field variable at j^{th} field node (x_j, y_j) is

$$F(x_j, y_j) = \begin{bmatrix} \boldsymbol{R}^T(r(x_j, y_j)) & \boldsymbol{P}^T(x_j, y_j) \end{bmatrix} \begin{bmatrix} \boldsymbol{A} \\ \boldsymbol{B} \end{bmatrix} \tag{26}$$

By assembling the above equation for all field nodes, the following matrix form is obtained

$$\boldsymbol{F}_0 = \boldsymbol{R}_0^T \boldsymbol{A} + \boldsymbol{P}_0^T \boldsymbol{B} \tag{27}$$

The detailed form of $\boldsymbol{R}_0$, $\boldsymbol{P}_0$ and vector $\boldsymbol{F}_0$ are given as follow.

$$\boldsymbol{F}_0 = \begin{bmatrix} F(x_1, y_1) & F(x_2, y_2) & ... & F(x_n, y_n) \end{bmatrix}^T \tag{28}$$

$$\boldsymbol{R}_0^T = \begin{bmatrix} r_1(x_1, y_1) & r_2(x_1, y_1) & \cdots & r_1(x_1, y_1) \\ r_1(x_2, y_2) & r_2(x_2, y_2) & \cdots & r_n(x_2, y_2) \\ \vdots & \vdots & \ddots & \vdots \\ r_1(x_n, y_n) & r_2(x_n, y_n) & \cdots & r_n(x_n, y_n) \end{bmatrix} \tag{29}$$

$$\boldsymbol{P}_0 = \begin{bmatrix} 1 & 1 & \cdots & 1 \\ x_1 & x_2 & \cdots & x_n \\ y_1 & y_2 & \ddots & y_n \\ \vdots & \vdots & \vdots & \vdots \end{bmatrix} \tag{30}$$

Notice that if there are n field nodes in the support domain and an *m*-term polynomial basis is used, there are *m*+*n* unknowns in vectors $\boldsymbol{A}$ and $\boldsymbol{B}$. In order to ensure that the solution of Eq. (27) is unique, the following constraint is assumed.

$$\boldsymbol{P}_0 \boldsymbol{A} = \boldsymbol{0} \tag{31}$$

With this constraint, Eq. (27) can be enriched as

$$\begin{bmatrix} \boldsymbol{F}_0 \\ \boldsymbol{0} \end{bmatrix} = \begin{bmatrix} \boldsymbol{R}_0^T & \boldsymbol{P}_0^T \\ \boldsymbol{P}_0 & \boldsymbol{0} \end{bmatrix} \begin{bmatrix} \boldsymbol{A} \\ \boldsymbol{B} \end{bmatrix} \tag{32}$$

By solving $\boldsymbol{A}$ and $\boldsymbol{B}$ from Eq. (32) and substituting them into Eq. (25), we have the expression of $F(x, y)$ which is

$$F(x, y) = \begin{bmatrix} \boldsymbol{R}^T(r(x, y)) & \boldsymbol{P}^T(x, y) \end{bmatrix} \begin{bmatrix} \boldsymbol{R}_0^T & \boldsymbol{P}_0^T \\ \boldsymbol{P}_0 & \boldsymbol{0} \end{bmatrix}^{-1} \begin{bmatrix} \boldsymbol{F}_0 \\ \boldsymbol{0} \end{bmatrix} \tag{33}$$

The first n terms of $\begin{bmatrix} \boldsymbol{R}^T(r(x,y)) & \boldsymbol{P}^T(x,y) \end{bmatrix} \begin{bmatrix} \boldsymbol{R}_0^T & \boldsymbol{P}_0^T \\ \boldsymbol{P}_0 & \boldsymbol{0} \end{bmatrix}^{-1}$ are the RPIM shape functions for the field nodes in the support domain, which can be used to construct interpolation functions for the integral point.

There are different types of RBFs such as multi-quadrics (MQ), Gaussian (EXP), thin plate spline (TPS) and Logrithmic. For simplicity, the TPS RBF

$$R(x,y) = r(x,y)^{\eta} \tag{34}$$

is used in this paper where η is the shape parameter.

2.4 Alpha shape method for tracking the boundary

As indicated in Section 2.2 and 2.3, a series of field nodes whose boundary is known at the un-deformed configuration will be generated firstly, if the CTM-RPIM is used. However, when the object undergoes large deformation the boundary will evolve accordingly. Hence, an efficient boundary identification method is essential. In this paper, the alpha shape method is adopted for boundary identification.

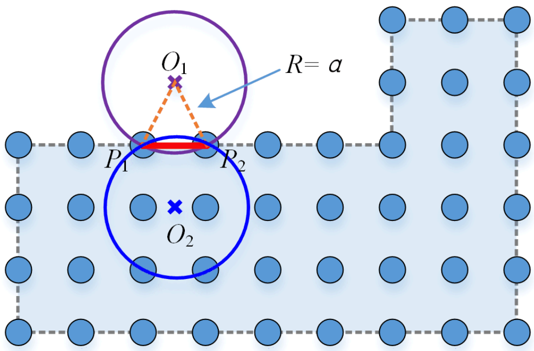

Fig. 5. Schematic diagram of alpha shape method

The basic idea of the alpha shape method is to check whether there is an empty circle of radius α passing through any two field nodes. If such a circle exists, the segment connecting the two field nodes is a boundary segment. The method can be implemented as follows (see Fig. 5):

(1) Calculate the length of line segment P_1P_2 consisting of any two field nodes P_1 and P_2.

(2) Compare the length of P_1P_2 with the preset circle diameter 2α;

(3) If P_1P_2 is less than 2α, draw two circles $\odot O_1$ and $\odot O_2$ with radius α passing through P_1

and P_2;

(4) If either circle is empty or with other nodes on the circle, line P_1P_2 is treated as a boundary segment;

(5) By repeating steps (1) – (4) for all combinations of field nodes, the boundary of the scattered field node cloud can be obtained.

The value of α sometimes has some influence on the tracking accuracy of the boundary, and some experiences can be referenced. In general, for regions of convex polygons, α can be larger, and for regions of concave polygons or with holes, α can be smaller. The boundaries of two sets of field nodes with complex boundaries have been identified using alpha shape method, as shown in Fig. 6.

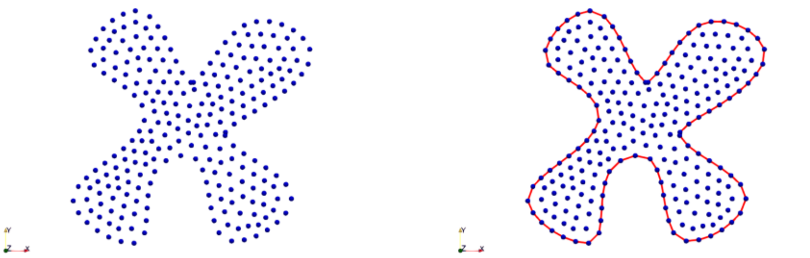

(a)

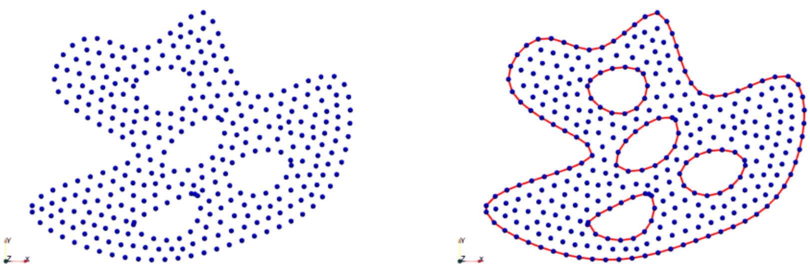

(b)

Fig. 6 Results of boundary identification (a) Problem domain without hole; (b) Problem domain with holes.

As can be seen from Fig. 6, the boundary identified by alpha shape method has reflect the shape of the problem domain well. Predictably, using the alpha shape method, the boundary can be recognized automatically in the simulation regardless of the large change of geometry. This enables the adaption of the method for analyzing large deformation problems.

3. Numerical examples

In this section, the influence of key parameters on the simulation results of the adaptive CTM-RPIM is investigated by simulating a cantilever beam subjected to small deformations. Thereafter, the precision of the adaptive CTM-RPIM for large deformation analysis is verified via modelling cantilever beams with large deformations. Moreover, the ability of evaluating the stability of geotechnical structures is tested using a slope and a foundation as benchmark examples. Finally, a 2-D soil collapse experiment is simulated using this method, which further demonstrates the capability of solving practical geotechnical problems.

3.1. Discussions on the selection of key parameters

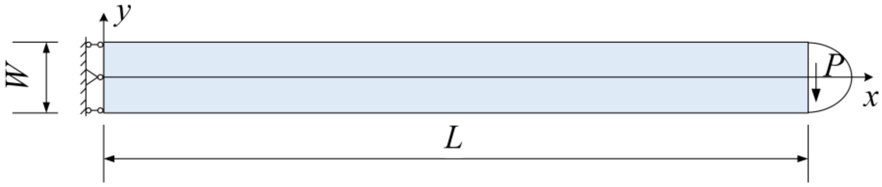

Fig. 7. The cantilever beam with parabolic load on the right end

The first example considered is a cantilever beam with a downward load of parabolic distribution on the right end, as shown in Fig. 7 [25, 26]. The analytical solution of the vertical displacement is

$$\Delta_y = \frac{P}{6EI}(3\mu y^2(L-x)+(4+5\mu)\frac{W^2 x}{4}+(3L-x)x^2) \tag{35}$$

where P is the force on the right end, E is the Young's modulus, μ is the Poisson's ratio, W is the width of the beam, L is the length of the beam, x and y are the coordinates. The values of these parameters are illustrated in Table 1.

Table 1. The parameters for the beam

P	E	μ	W	L
-1000Pa	3×10^7Pa	0.3	12m	48m

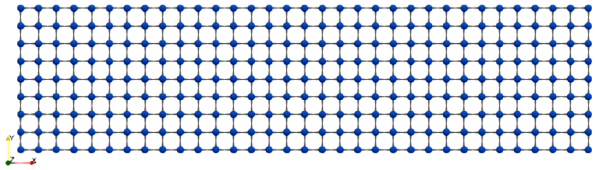

(a)

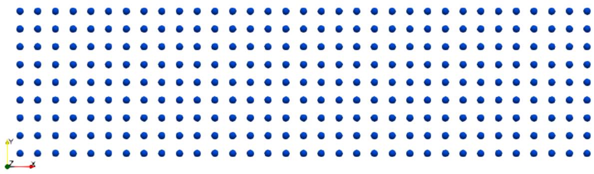

(b)

Fig. 8. The model of FEM and CTM-RPIM (33×9 nodes) (a) FEM model; (b) CTM-RPIM model

The accuracy of the CTM-RPIM is first verified against the simulation result from FE modelling with different density levels of nodes. Then the most influential factors are investigated, which are the width between two adjacent integral lines r_y, the length of sub-segment for integration r_x, the radius of support domain r_c and the shape parameter of RPIM η. To measure the distance r_x, r_y and r_c, the mean node spacing d_c is defined

$$d_c = \frac{\sqrt{A}}{\sqrt{n}-1} \tag{36}$$

where A is the area of problem domain and n is the total number of field nodes.

The vertical displacements at the right end of the beam from the FEM and CTM-RPIM modelling are shown in Fig. 9. The total number of nodes used in the FEM and CTM-RPIM simulations is the same (Fig. 8). The four-node element is used in FEM (Fig. 8 (a)) while, in the CTM-RPIM simulation, we have $\eta = 5.0$, $r_c = 2.0d_c$, and two integration points are used for each integral sub-segment.

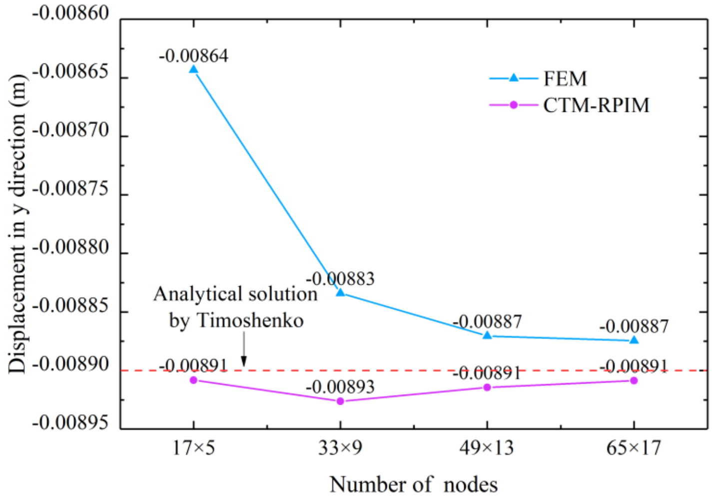

(a)

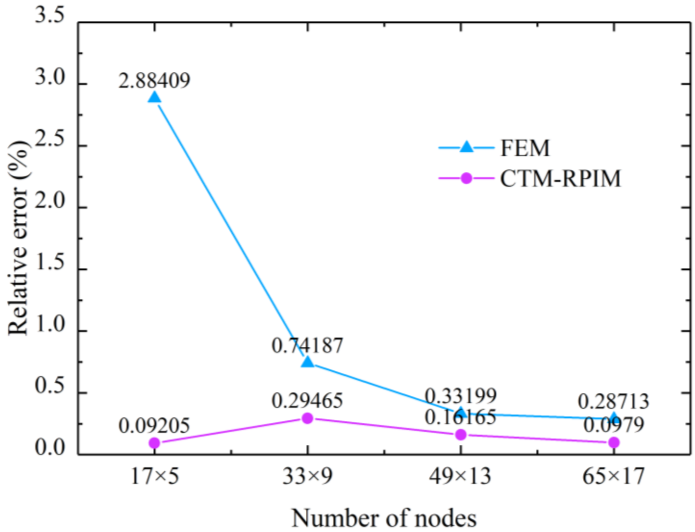

(b)

Fig. 9. Results of vertical displacement at the right end of the cantilever beam (a) The vertical displacement at the right end of the beam; (b) The relative error of the calculated vertical displacement versus the number of used nodes

As seen in Fig. 9, if the parameters are chosen appropriately, the accuracy of CTM-RPIM can be much higher than that of FEM at all field nodes density level, because that RPIM shape functions are high order and have a larger support domain. Even when a cloud of field nodes with loose density is used, the relative error is still low. The maximum relative error of CTM-RPIM is only about 0.3%. Additionally, the integral points used in CTM-RPIM is less than that of FEM. The ratio between the numbers of integration points used in CTM-RPIM and the FEM is $\frac{a}{2(a-1)}$ where a is the number of nodes in y direction.

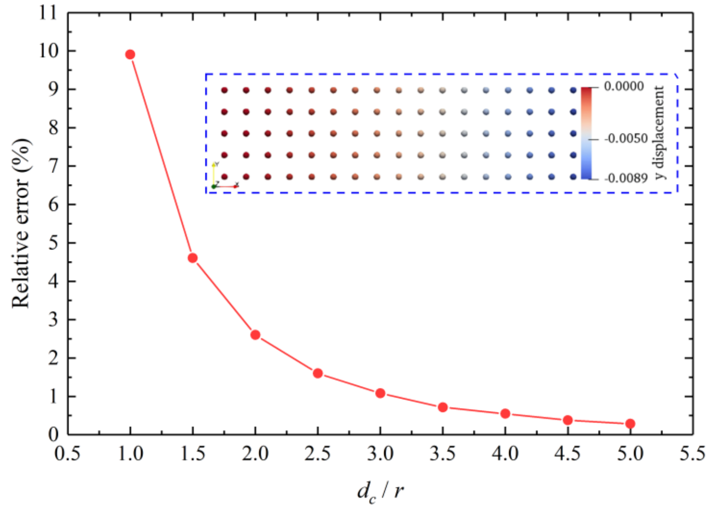

(a)

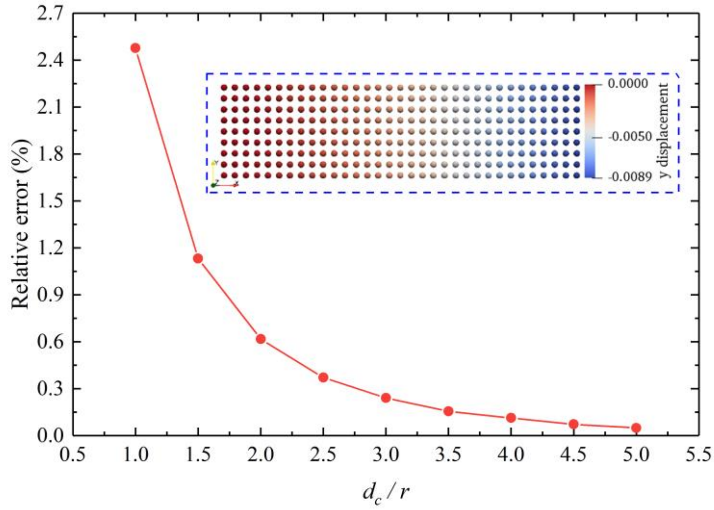

(b)

Fig. 10. The influence of r_x and r_y (a) Results of 17×5 nodes; (b) Results of 33×9 nodes

The influence of the number of integral points on the CTM-RPIM simulation is studied in this section. Two sets of field nodes, namely 17×5 and 33×9, are used in the simulation with $r_x = r_y = r$. A sufficiently large radius of support domain is selected which is $r_c = 4.0d_c$. The shape parameter is set to 5.0. Only one integral point is used for each integral sub-segment, which means that the number of used integral points depends on the length r. To study the influence of the integral points, the ratio d_c / r varies from 1.0 to 5.0 with an interval of 0.5. The simulation results are shown in Fig. 10. As expected, the accuracy is improved with the increase of d_c / r and the convergence rate is roughly exponential. When d_c / r is greater than or equal to 3.0, a satisfactory accuracy is obtained.

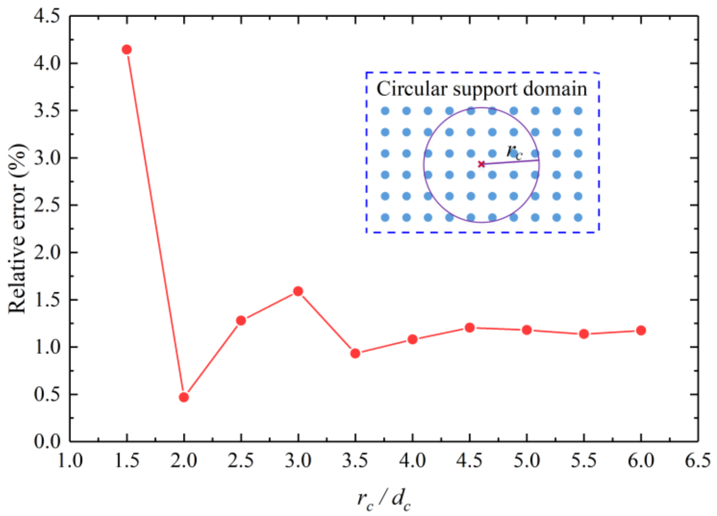

Fig. 11. The influence of support domain radius r_c

The size of support domain is another factor influencing the CTM-RPIM simulation. A larger support domain implies that more field nodes contribute in the construction of shape functions which leads to higher accuracy. However, the computational cost also rises because of the increase in the involved field nodes. Therefore, it is essential to investigate the size of a support domain in relation to the simulation accuracy and computational cost. As a circular support domain is adopted in this work, the non-dimensional radius of the support domain r_c / d_c is the indicator of its size which has been varied from 1.5 to 6.0 with an interval 0.5 in this study. The layout of field nodes is 17×5, the shape parameter η is set to 5.0, the distance r_x and r_y are set to $\frac{1}{3}d_c$, and one integral point is used for each sub-segment. As can be seen from Fig.11, when the radius $r_c \geq 3.5d_c$, the relative error is less than 1.5% and nearly stable regardless of the increase of r_c / d_c. Thereby, the recommended range of the radius of a support domain is between $3.5d_c$ and $4.0d_c$.

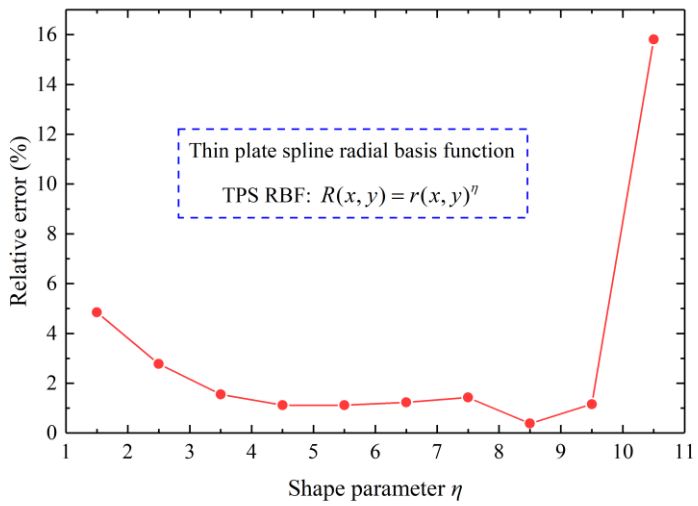

Fig. 12. The influence of shape parameter η

Finally, the effect of the shape parameter η of TPS RBF on the simulation is explored. To this end, the shape parameters from 1.5 to 10.5 with an interval 1.0 are adopted in the simulation, and other parameters are $r_x = r_y = \frac{1}{3} d_c$ and $r_c = 4.0 d_c$. A cloud of filed nodes 17×5 is used to discretize the problem domain and one integral point is assigned to each segment. Fig. 12 shows that the value of η in the range of [3.5, 9.5] leads to higher accuracy, and the relative error is low and stable when η is between 4.5 and 7.5.

3.2. Large deformation analysis of cantilever beam

In this section, the ability of the adaptive CTM-RPIM for dealing with large deformation problems is demonstrated. To this end, two linear-elastic cantilever beams undergo large deformations because of the imposed force (Fig. 13) and moment (Fig. 16) are concerned. The alpha shape method is used to identify the boundary of the problem domain, which makes the CTM-RPIM adaptive regardless of the change of geometry.

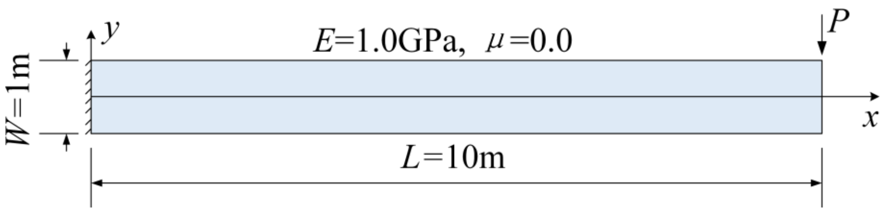

Fig. 13. The cantilever beam with concentrated force on the right end

The first case is a cantilever beam subjected to a downward concentrated load *P* as shown in Fig. 13. The length and the width of the beam are $L = 10\mathrm{m}$ and $W = 1\mathrm{m}$, respectively. The elastic constants are Young's modulus $E = 1.0\mathrm{GPa}$ and Poisson's ratio $\mu = 0.0$. A total of 306 field nodes are used in the simulation. The analytical solution of this problem is available in [27].

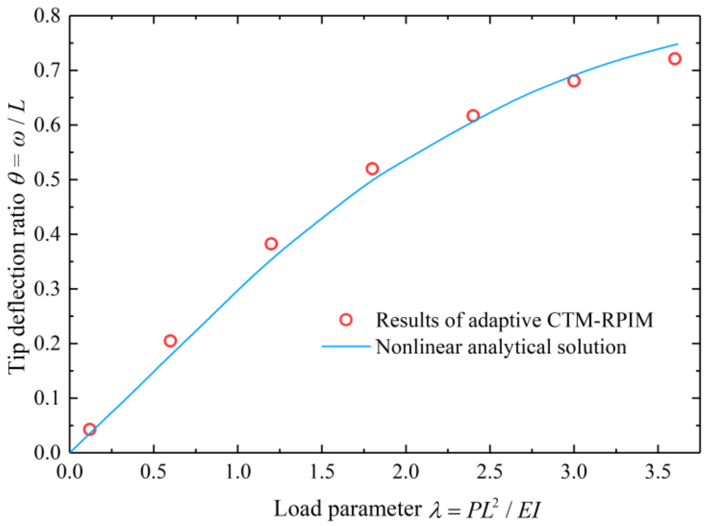

Fig. 14. The results at different levels of force *P*

To show the accuracy of the adaptive CTM-RPIM, a series of cases with different concentrated forces at the right-top corner are simulated with results compared to the nonlinear analytical solutions. The applied forces *P* are at different levels, namely 100kN, 500kN, 1000kN, 1500kN, 2000kN, 2500kN and 3000kN respectively. The curves of tip deflection ratio $\theta = \frac{\omega}{L}$, where ω is the deflection at the right end, versus the non-dimensional load parameter $\lambda = \frac{PL^2}{EI}$, where I is the inertia moment of beam section, are shown in Fig. 14. The configuration of the deformed cantilever beam at the concentrated force levels $P = 2000\mathrm{kN}$ and $P = 3000\mathrm{kN}$ are presented in Fig. 15. Clearly, the simulation results from the adaptive CTM-RPIM agree well with the analytical solution from [27], which demonstrates the correctness of the adaptive CTM-RPIM for analyzing large deformation problems.

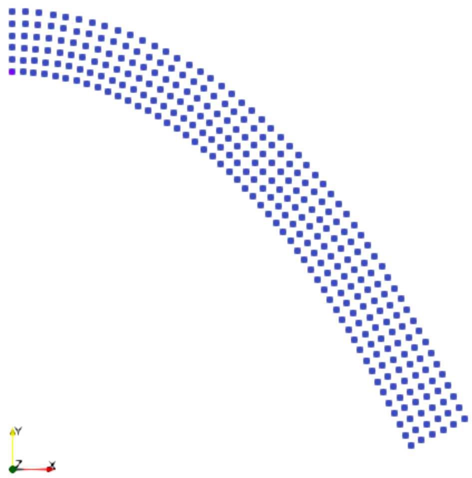

(a)

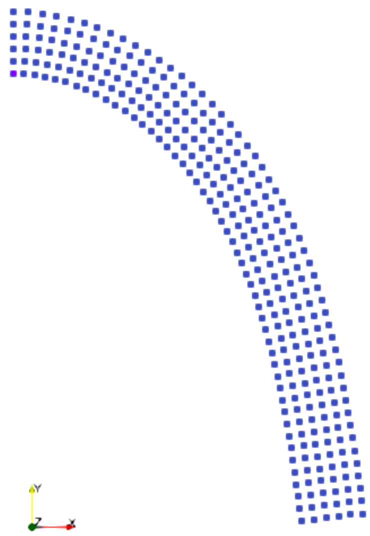

(b)

Fig. 15. The final configuration of the beam at two different force levels (a) $P = 2000\text{kN}$; (b) $P = 3000\text{kN}$

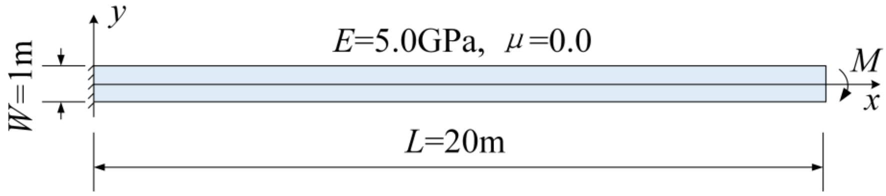

Fig. 16. The cantilever beam with bending moment on the right end

A cantilever beam subjected to a bending moment at the right end is studied in this section. The setup of the problem is shown in Fig. 16. According to the nonlinear analytical solution given by Pai and Palazotto [28], when an appropriate bending moment is applied at the right end, the cantilever beam will bend into a perfect circular ring. The bending moment M to make the beam achieve this state can be determined by

$$M = \frac{2\pi EI}{L} \tag{37}$$

In the simulation, the moment is transformed into two uniform loads applied to the upper and lower halves of the beam end section according to [29]. A total of 405 field nodes are used to discretize the problem domain and 1000 incremental analysis steps are adopted. The deformation process of the cantilever beam obtained from the adaptive CTM-RPIM is shown in Fig. 17. A near perfect circular ring is obtained when the moment calculated from Eq. (37) is enforced at the end of the beam which verifies the proposed method for large deformation analysis.

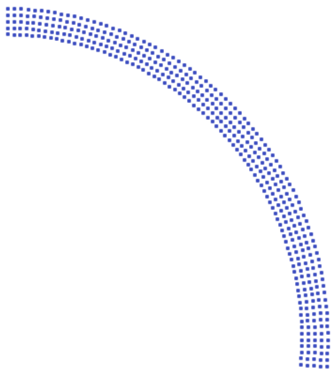

(a)

(b)

(c)

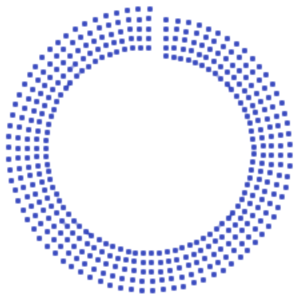

(d)

Fig. 17. The deformation process of the beam (a) 250 steps; (b) 500 steps; (c) 750 steps; (d) 1000 steps

3.3. Quasi static analysis of stability problem

Stability analysis is of great importance in geotechnical engineering, which must be carried out to ensure the geotechnical structures won't failure before and after they are finished. To evaluate the capability of adaptive CTM-RPIM in analyze the stability, two classical benchmark examples have been studied in this section. The first example is to evaluate the stability of a slope and the second is to calculate the bearing capacity of a foundation. These two examples fully demonstrate the reliability of this method in the stability analysis of geotechnical engineering.

3.3.1 Slope stability analysis

In this section, a homogeneous soil slope is studied with the strength reduction method, and the obtained safety factor is used to verify its reliability. The geometry of the slope is given in Fig. 18, and the material properties are Young's modulus $E = 100\mathrm{MPa}$, Poisson's ratio $\mu = 0.3$, cohesion $c = 10\mathrm{kPa}$, friction angle $\Phi = 20°$, dilatancy angle $\Psi = 0.001°$ and the unit weight $\gamma = 20\mathrm{kN/m^3}$.

The bottom of the slope is fully fixed while the lateral boundaries are fixed horizontally. The elastic-perfectly plastic constitutive model with Mohr-Coulomb yield criterion is used adopted. A total of 1881 field nodes are used in the CTM-RPIM simulation.

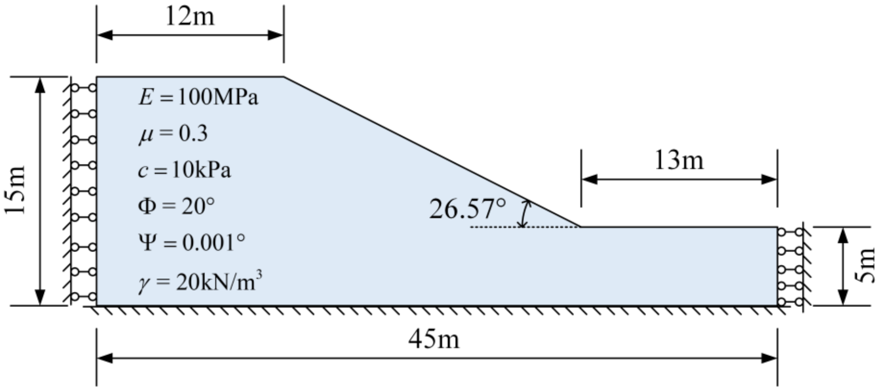

Fig. 18. The homogeneous slope

The formulation of the strength reduction method [30] can be expressed as

$$c' = \frac{c}{SRF} \tag{38}$$

$$\Phi' = arctan(\frac{tan(\Phi)}{SRF}) \tag{39}$$

where c' and Φ' are the material parameters after strength reduction, and SRF is the reduction factor.

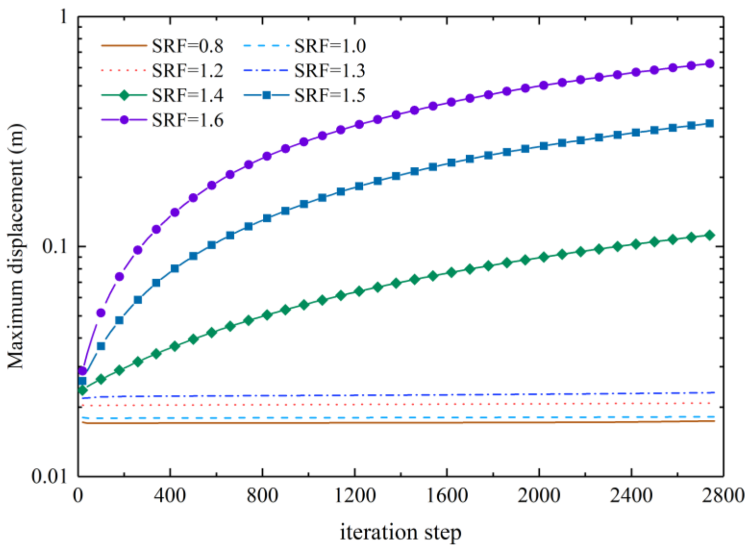

(a)

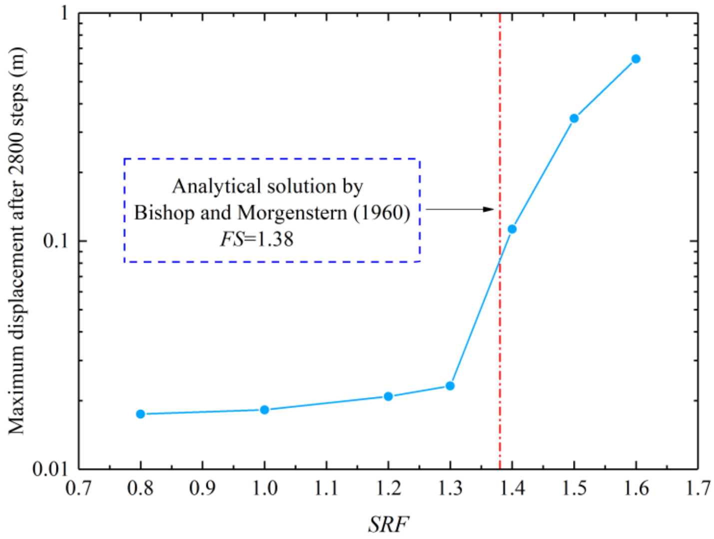

(b)

Fig. 19. The maximum displacement of the slope (a) Maximum displacement for every step; (b) Final maximum displacement after 2800 steps

The reduction factor *SRF* ranging from 0.8 to 1.6 is used with simulation results after a large enough step (2800 steps) illustrated in Fig. 19 (a) and (b). Fig. 19 (a) shows that the deformation is negligible when $SRF \leq 1.3$. In contrast, the displacement increases continuously and convergence cannot be achieved for $SRF \geq 1.4$. In other words, when $SRF \leq 1.3$ the slope is stable and when $SRF \geq 1.4$ the slope is unstable. The same conclusion can also be obtained by showing the curve of the displacement against SRF (see Fig. 19 (b)). Hence, it is clear that the safety factor *FS* of the slope is within (1.3, 1.4), which embraces the analytical solution 1.38 provided by Bishop and Morgenstern [31].

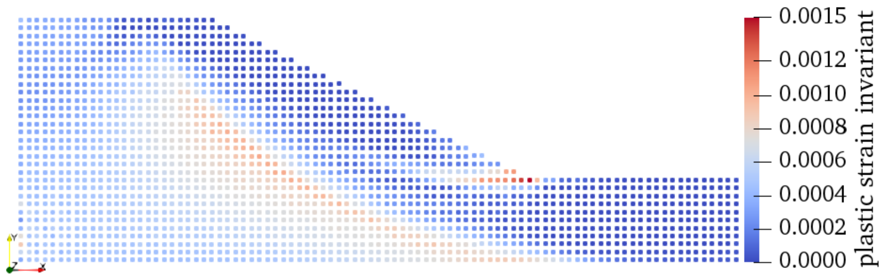

(a)

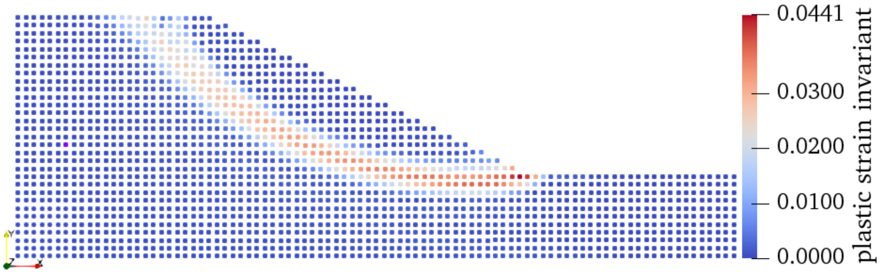

(b)

Fig. 20. The plastic strain invariant of the slope after 2800 steps (a) *SRF* = 1.3; (b) *SRF* = 1.4

Further, to insight why the slope loses stability, the counter of plastic strain invariant of the cases $SRF = 1.3$ and $SRF = 1.4$ are given in Fig. 20. It can be seen that, when the *SRF* is 1.3 the plastic strain is very small, areas of plasticity are isolated from each other and have not penetrated the whole slope. However, when the *SRF* is 1.4, the plastic area is connected and form a clear shear band and the soil slides down along the shear band to eventually form a landslide.

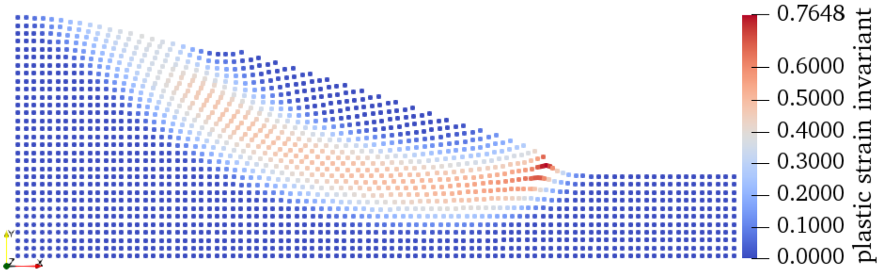

Fig. 21.The result of *SRF* = 1.6 after 10000 steps

Finally, a large deformation case *SRF*=1.6 after 10000 steps is given in Fig. 21. It preliminarily shows the ability of this method to deal with large deformations, when large deformation occurs, the shear band is still clearly visible without numerical instability

3.3.2 Bearing capacity analysis

A flexible strip footing on weightless soil in semi-infinite space is studied in this section, of which the bearing capacity is analyzed to test its precision, as shown in Fig. 22 (a). The analytical solution of this classical problem was found by Prandtl in 1920 [32]

$$q_{failure} = (2+\pi)c_u \quad (40)$$

where c_u is the undrained shear strength of the soil.

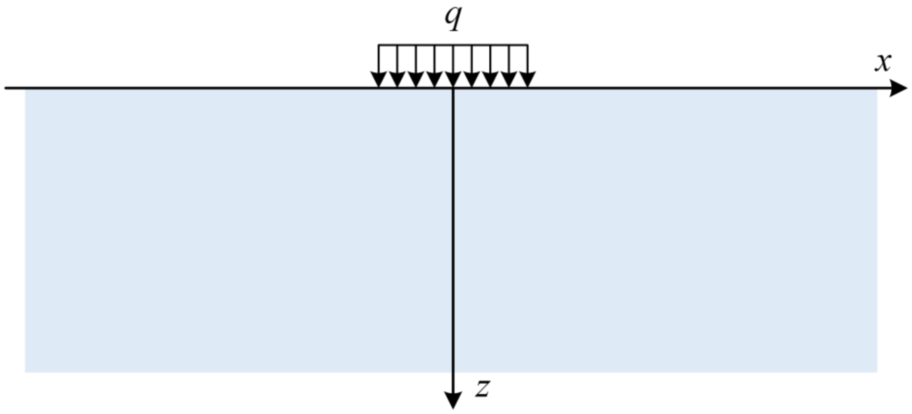

(a)

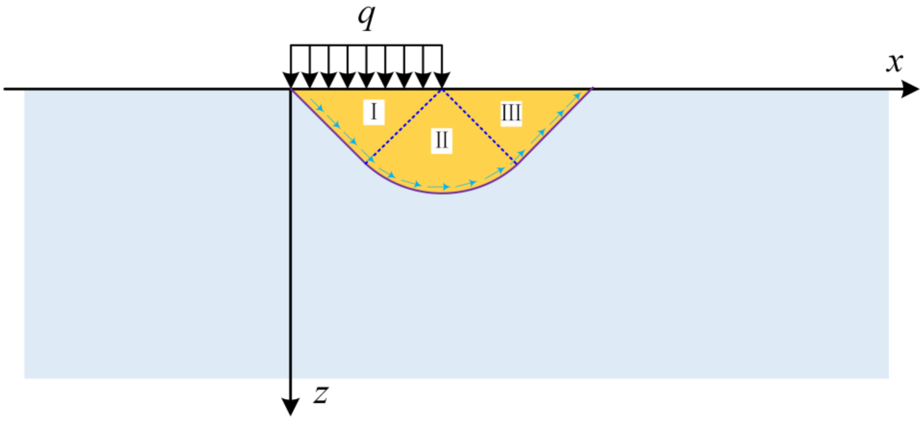

(b)

Fig. 22. The flexible strip footing on weightless soil (a) Description of the problem; (b) Prandtl's schematization [32]

The simplified model is given in Fig. 23, the scale is 12m × 5m, the loaded width is 2m, and the boundary conditions are rollers at both side directions and fixed at the bottom. Elastic-perfect plastic constitutive and Mohr-Coulomb yield criterion are used in this example, and the material properties are as follows. Young's modulus $E = 100\text{MPa}$, Poisson's ratio $\mu = 0.3$, the undrained cohesion $c_u = 100\text{kPa}$, friction angle Φ and dilatancy angle Ψ are both set to $0.001°$ and density ρ is chosen as $0.0\text{kg}/\text{m}^3$. A model with 1029 field nodes is generated to solve this problem, and the result is given in Fig. 24.

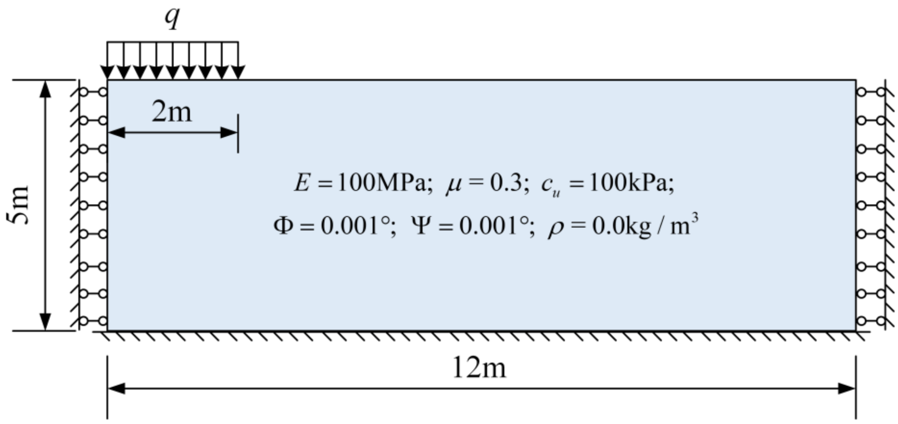

Fig. 23. Symmetry-based simplification for numerical simulation

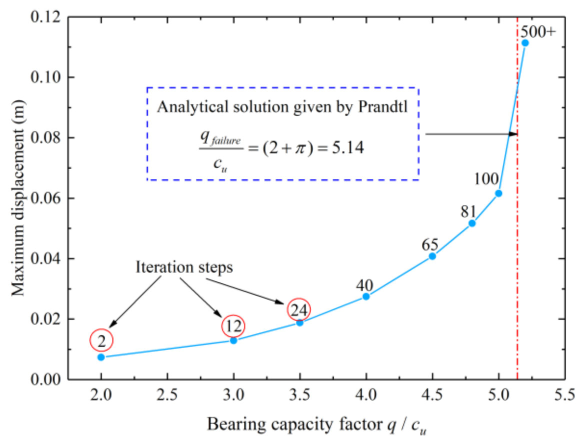

Fig. 24. Plot of maximum displacement versus bearing stress

At different load levels from 200kN to 520kN, the convergence should occur with few iteration steps and small deformation if the strip footing is stable. As can be seen from Fig. 24, when the load is less than or equal to 500kPa, the convergence can be achieved quickly within 100 iteration steps, and the maximum deformation at all load levels is about 6 cm. But when the load reaches 520kPa, the convergence cannot be attained within 500 iterations, and the displacement at 500 steps shown in Fig. 24 is about 11cm, which is nearly two times of that at 500kPa. That means the failure load of the flexible strip footing is between 500kPa and 520kPa, including Prandtl's solution of 514kPa. That is, adaptive CTM-RPIM is reliable in the evaluation of the bearing capacity of the flexible strip footing. If a more accurate result is required, a more refined numerical model can be used.

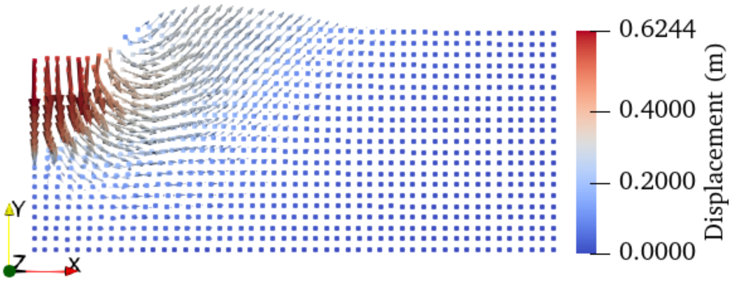

Fig. 25. The displacement at the load level of 540kPa

The deformed configuration at 540kPa is given in Fig. 25, where the deformation reaches over 0.6 m, and the failure mechanism proposed by Prandtl shown in Fig. 22 (b) can be easily seen from the deformation trend displayed by arrows with direction in Fig. 25. Again, it is verified that the adaptive CTM-RPIM has great advantages in stability evaluation and the deformation trend prediction.

3.4 Dynamic analysis of post failure problem

In order to further test the ability of this method for solving geotechnical large deformation problems, the soil collapse process was simulated. It is a 2-D experiment carried out by Ha H. Bui et al. [33], where the soil particles are modeled by many small aluminum bars, as shown in Fig. 26. Constrained by a movable baffle, these bars are initially stacked into a rectangular column. At the beginning of the test, the baffle was quickly removed, and the soil column collapsed rapidly under its own weight. After a long run out distance, it accumulated into an approximate triangle area. The parameters of soil are given as: Young's Module $E = 0.84\text{MPa}$, Poisson's ratio $\mu = 0.3$, cohesion $c = 0\text{MPa}$, friction angle $\Phi = 19.8°$, dilatancy angle $\Psi = 0.001°$ and density $\rho = 2650\text{kg}/\text{m}^3$.

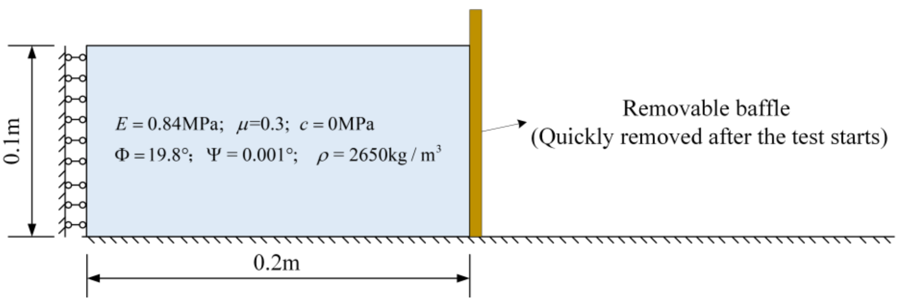

Fig. 26. 2-D experiment of soil collapse [33].

The numerical model was discretized into 1071 field nodes, and elastic-perfect plastic constitutive and Mohr-Coulomb yield criterion are used. The boundary conditions are set as fixed at the bottom boundary and rolling at the left boundary, following the settings given in [33, 34]. Because the collapse of soil column is very fast and the deformation is extremely large, the inertia force is not negligible, the dynamic scheme is adopted here. The time step is chosen as $\Delta t = 5.0\mu s$, which is small enough to ensure the stability and accuracy of calculation.

(a)

(b)

(c)

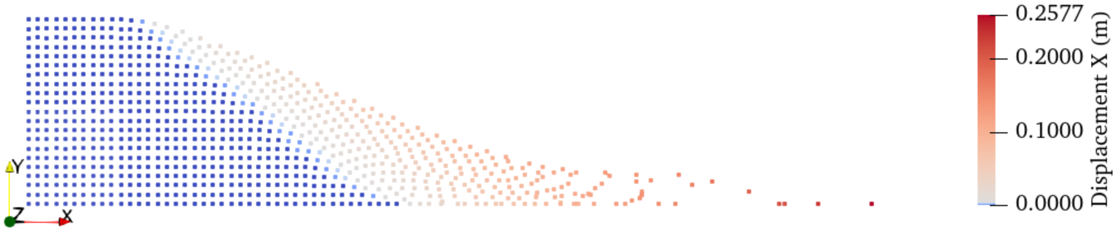

(d)

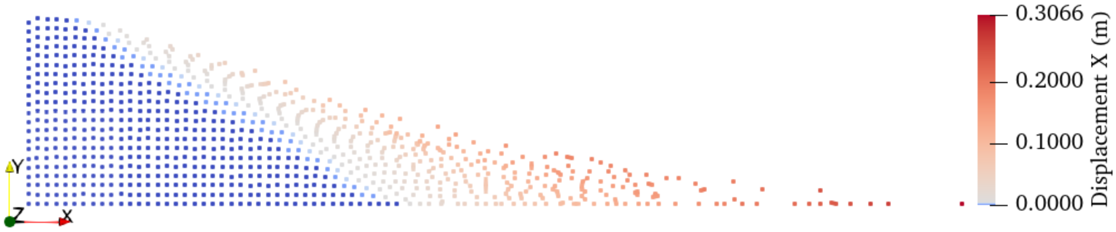

(e)

Fig. 27. Collapse process of soil column (a) Initial configuration; (b) Configuration at 0.1s; (c) Configuration at 0.2s; (d) Configuration at 0.3s; (e) Final configuration.

The collapse process of soil column is given in Fig. 27, in which field nodes are rendered in different colors depending on the displacement to observe the deformation inside the soil column. After the baffle is removed, the soil column immediately begins to collapse, and the soil on the upper right begins to slide, while the soil on the lower left remains static. As time goes on, the static region decreases gradually. At the end of the collapse process, the soil particles stop moving, the upper surface of the accumulation is at an angle slightly less than the friction angle, and a small region remains static in the lower left corner. The interface between the static region and sliding region is what we call sliding surface.

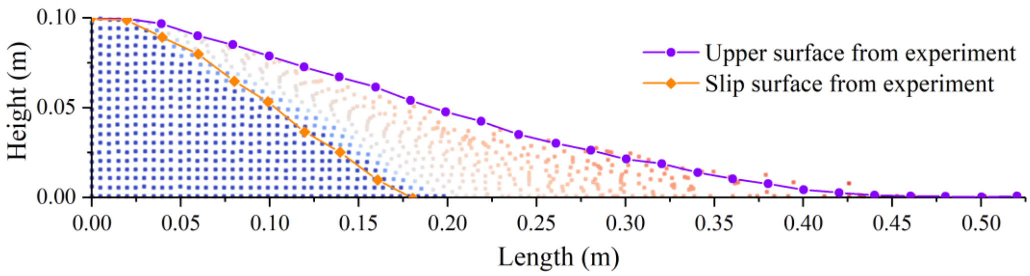

Fig. 28. Final configuration of the soil collapse example

Finally, the final upper surface and the sliding surface are compared with the experimental observations, which is presented in Fig. 28. It can be clearly seen that the numerical result agrees well with the experimental result, which can further demonstrate the ability of adaptive CTM-RPIM for simulating geotechnical large deformation problems.

4. Conclusions

An adaptive CTM-RPIM for solving geotechnical large deformation problems is introduced in this paper. Using CTM and RPIM, the domain integration can be transformed into line integration and the interpolation can get rid of the restraints from the background mesh. Meanwhile, to handle large deformation problems more conveniently, the alpha shape method is introduced to track the boundary automatically, with the results shown accurate and convenient. For the purpose of facilitating programming, both quasi static version and dynamic version of computational processes are given. Moreover, the influence of key parameters on precision is explored systematically, and the recommend values of these parameters are given in this paper. Then, two geotechnical examples, slope and footing, are analyzed to further demonstrate the accuracies and reliabilities of the method. Finally, by simulating the 2-D soil collapse experiment with a large run out distance, the capacity of dealing with large deformations is further proved. To sum, the adaptive CTM-RPIM is a promising method and has great potential in the application of geotechnical engineering.

Acknowledgements

The authors wish to acknowledge the National Natural Science Foundation of China (Grant Nos. 51979270 and 51709258), and the CAS Pioneer Hundred Talents Program for their financial supports of the authors.

Reference

[1]. Cruden D M. A simple definition of a landslide. B Eng Geol Environ 1991; 43: 27–29.

[2]. Hungr O, Leroueil S, Picarelli L. The Varnes classification of landslide types, an update. Landslides 2014; 11(2): 167–194.

[3]. Locat A, Leroueil S, Bernander S, Demers D, Jostad H P, Ouehb L. Progressive failures in eastern Canadian and Scandinavian sensitive clays. Can Geotech J 2011; 48(11): 1696–1712.

[4]. Cheng L, Liu YR, Yang Q, Pan YW, Lv Z. Mechanism and numerical simulation of reservoir slope deformation during impounding of high arch dams based on nonlinear FEM. Comput Geotech 2017; 81: 143-54.

[5]. Török Ákos, Barsi Arpad, Bögöly Gyula, Lovas Tamas, Somogyi Arpad, Görög Péter. Slope stability and rockfall assessment of volcanic tuffs using RPAS with 2-D FEM slope modelling. Nat Hazard Earth Sys 2018; 18(2): 583-97.

[6]. Gülnihal Meral, M Tezer-Sezgin. DRBEM solution of exterior nonlinear wave problem using FDM and LSM time integrations. Eng Anal Bound Elem 2010; 34(6): 574-80.

[7]. Rao X, Cheng LS, Cao RY, Jiang J, Li N, Fang SD, Jia P, Wang LZ. A novel green element method by mixing the idea of the finite difference method. Eng Anal Bound Elem 2018; 95: 238-47.

[8]. Yerro Alba, Alonso Eduardo, Puigmartí Núria. The material point method for unsaturated soils. Géotechnique 2015; 65(3): 201-17.

[9]. Nairn John. Modeling Imperfect Interfaces in the Material Point Method using Multimaterial Methods. Cmes Comp Model Eng 2013; 92(3): 271-99.

[10]. Pathania Tinesh, Bottacin-Busolin Andrea, Rastogi A, Eldho T I. Simulation of Groundwater Flow in an Unconfined Sloping Aquifer Using the Element-Free Galerkin Method. Water Resour Manag 2019; 33(2): 2827-45.

[11]. Azher Jameel, G A Harmain. Fatigue crack growth in presence of material discontinuities by EFGM. Int J Fatigue 2015; 81: 105-16.

[12]. Mohit Pant I V Singh, B K Mishra. Evaluation of mixed mode stress intensity factors for interface cracks using EFGM. App Math Model 2011; 35(7): 3443-59.

[13]. A Abdollahifar, M R Nami, A R Shafiei. A new MLPG method for elastostatic problems. Eng Anal Bound Elem 2012; 36(3): 451-57.

[14]. Khosravifard Amir, Hematiyan M. A new method for meshless integration in 2-D and 3-D Galerkin meshfree methods. Eng Anal Bound Elem 2010; 34: 30-40.

[15]. Kazemi Zahra, Hematiyan M, Vaghefi Reza. Meshfree radial point interpolation method for analysis of viscoplastic problems. Eng Anal Bound Elem 2017; 82: 172-84.

[16]. Hematiyan M, Khosravifard Amir, Liu GR. A background decomposition method for domain integration in weak-form meshfree methods. Compute Struct 2014; 142: 64–78.

[17]. Li Y, Liu GR, Yue J. A novel node-based smoothed radial point interpolation method for 2-D and 3-D solid mechanics problems. Comput Struct 2018; 196: 157-72.

[18]. Gu YT. An enriched radial point interpolation method based on weak-form and strong-form. Mech Adv Mater Struct 2011; 18(8): 578-84.

[19]. Liu GR, L Yan, Wang JG, Gu YT. Point interpolation method based on local residual formulation using radial basis functions. Struct Eng Mech 2002; 14(6): 713-32.

[20]. Zhang, X., Krabbenhoft, K., Pedroso, D. M., Lyamin, A. V., Sheng, D., da Silva, M. V., & Wang, D. (2013). Particle finite element analysis of large deformation and granular flow problems. COMPUTERS AND GEOTECHNICS, 54, 133-142.

[21]. Monforte L, Arroyo M, Carbonell J M, Gens A. Numerical simulation of undrained insertion problems in geotechnical engineering with the particle finite element method (PFEM). Comput

Geotech 2017; 82(Feb): 144–56.

[22]. Zhang W, Zhong ZH, Peng C, Yuan WH, Wu W. GPU-accelerated smoothed particle finite element method for large deformation analysis in geomechanics. Comput Geotech 2021; 129:103856.

[23]. Jin YF, Yin Zy, Yuan Wh. Simulating retrogressive slope failure using two different smoothed particle finite element methods: A comparative study. Eng Geol 2020; 279: 105870.

[24]. Meng, J., Zhang, X., Utili, S., & Oñate, E. (2021). A nodal-integration based particle finite element method (N-PFEM) to model cliff recession. Geomorphology, 381, 107666.

[25]. Yang YT, Sun GH, Zheng H, Fu XD. A four-node quadrilateral element fitted to numerical manifold method with continuous nodal stress for crack analysis. Compute Struct 2016; 177: 69-82.

[26]. Xu DD, Yang YT, Zheng H, Wu AQ. A high order local approximation free from linear dependency with quadrilateral mesh as mathematical cover and applications to linear elastic fractures. Compute Struct 2017; 178: 1-16

[27]. Zhao GF. Development of the distinct lattice spring model for large deformation analyses. Int J Numer Anal Met 2014; 38: 1078-100.

[28]. Pai P F, Palazotto A N. Large-deformation analysis of flexible beams. Int J Solids Struct 1996; 33(9): 1335–70.

[29]. Zhang W, Yuan WH, Dai BB. Smoothed Particle Finite-Element Method for Large-Deformation Problems in Geomechanics. Int J Geomech 2018; 18(4): 04018010.

[30]. Ma YC, Su PD, Li YG. Three-dimensional nonhomogeneous slope failure analysis by the strength reduction method and the local strength reduction method. Arab J Geosci 2020; 13(2): 1-7.

[31]. Bishop A W, Morgenstern N R. Stability coefficients for earth slopes. Géotechnique 1960; 10(4): 129-47.

[32]. L Prandtl. Über die Härte plastischer Körper. Nachrichten von der Gesellschaft der Wissenschaften zu Göttingen, Mathematisch-physikalische Klasse 1920; 74–85.

[33]. Bui HH, Fukagawa R, Sako K, Ohno S. Lagrangian meshfree particles method (SPH) for large deformation and failure flows of geomaterial using elastic-plastic soil constitutive mode. Int J Numer Anal Met 2010; 32(12): 1537-70.

[34]. Lian YP, Zhang X, Liu Y. An adaptive finite element material point method and its application in extreme deformation problems. Comput Method Appl M 2012; 241-24: 275-85.